Canadian Science Publishing | Canadian Geotechnical Journal

Pressure-Driven Variations in CO_2 Displacement Patterns within Heterogeneous Porous Structures: A High-Pressure Microfluidic Study

Journal:	*Canadian Geotechnical Journal*
Manuscript ID	cgj-2025-0433.R1
Manuscript Type:	Note
Date Submitted by the Author:	02-Oct-2025
Complete List of Authors:	Zhang, Jinyong; Zhejiang University Lu, Zhao; Hainan Institute of Zhejiang University Hong, Yi; Zhejiang University Wang, Li-Zhong; Zhejiang University Gan, Yixiang; The University of Sydney Yan, Mengqiu; Zhejiang University
Is the manuscript for consideration in a Special Issue or Collection?:	Not applicable (regular submission)
Keyword:	CO2 Geological Storage, Microfluidic Study, Displacement Patterns, CO2 Saturation, Fractal Dimension

SCHOLARONE™
Manuscripts

© The Author(s) or their Institution(s)

Pressure-Driven Variations in CO_2 Displacement Patterns within Heterogeneous Porous Structures: A High-Pressure Microfluidic Study

Jinyong Zhang [a], Zhao Lu [b], Yi Hong [a, *], Lizhong Wang [a, *], Yixiang Gan [c], Mengqiu Yan [d]

[a] Key Laboratory of Offshore Geotechnics and Material of Zhejiang Province, College of Civil Engineering and Architecture, Zhejiang University, Hangzhou, 310056, China

[b] Hainan Institute of Zhejiang University, Sanya, 572025, China

[c] School of Civil Engineering, The University of Sydney, NSW 2006, Australia

[d] Ocean College, Zhejiang University, Zhoushan, 316021, China

* Corresponding author. Yi Hong and Lizhong Wang

Email address: yi_hong@zju.edu.cn; wanglz@zju.edu.cn

Draft

© The Author(s) or their Institution(s)

Abstract

The displacement patterns of CO_2 are critical for assessing the storage capacity and efficiency of geological CO_2 sequestration, yet they remain underexplored across different pressures. For this purpose, an advanced high-pressure and high-temperature microfluidic platform is developed. By integrating a high-pressure chamber equipped with an observation window and high-strength glass chips, it is capable of operating at pressures up to 50 MPa and enables real-time observation of CO_2 displacement patterns at the pore scale. Experiments conducted across a pressure range from 1 bar to 16 MPa that enables the analysis of changes in displacement patterns, CO_2 saturation, displacement front length, and fractal dimension within heterogeneous porous media. The findings reveal that at low pressures and a flow rate of 0.1 mL/min, CO_2 displacement was predominantly influenced by capillary forces, resulting in preferential invasion of larger pore throats. In contrast, at higher pressures, the displacement process was dominated by the synergistic effects of the viscous and capillary forces of supercritical CO_2. This results in the breakthrough of the main flow channel on the outlet side and tributary structures spanning its width on the inlet side. The platform offers robust means to investigate CO_2 displacement efficiency and optimize storage strategies.

Draft

Keywords: CO_2 Geological Storage; Microfluidic Study; Displacement Patterns; CO_2 Saturation; Fractal Dimension.

1. Introduction

Carbon dioxide geological storage (CGS) stands as a premier strategy for significantly mitigating atmospheric greenhouse gas concentrations. In CGS, the injection of CO_2 into deep saline aquifers will displace the native brine within the porous rock matrix. Ensuring the safety and efficiency of CO_2 sequestration is of critical importance for its long-term viability (Goodman et al. 2011). Extensive research has demonstrated that the lower viscosity of supercritical CO_2 relative to reservoir brine results in

© The Author(s) or their Institution(s)

displacement instability, which substantially reduces the effectiveness of CO_2 sequestration (Berg and Ott 2012; Wang et al. 2013). Moreover, the unstable fingering flow of CO_2 combined with the inherent microcracks in the rock (Jiang et al. 2021; Li et al. 2020) elevates the risk of premature breakthrough (Song et al. 2012), which in turn increases the probability of CO_2 leakage. Consequently, a thorough understanding and monitoring of CO_2-water displacement dynamics within porous media are crucial to ensuring the long-term stability and security of CO_2 sequestration (Doughty 2010; Juanes et al. 2010).

As a powerful technology to study the microscopic behaviour of fluids, microfluidics is widely used in various fields, including the enhancement of oil recovery (Saadat et al. 2021; Yu et al. 2023; Zhang et al. 2023), the extraction of gas hydrates (Wang et al. 2021; Yao et al. 2022; Zhang et al. 2024), drug development (Liu et al. 2021), microbial engineering (Ho et al. 2020), CGS (Hu et al. 2017; Kim et al. 2012; Song et al. 2020; Zeng et al. 2025; Zheng et al. 2017), and the infiltration of water into the ground due to rainfall (Li et al. 2024; Zhan et al. 2021). The microchannels on chips, sized from a few microns to several hundred microns, offer advantages like small volume, large specific surface area, and significant surface tension. They allow for real-time visual observation of changes in fluid morphology within tiny channels, providing robust evidence for researchers to investigate microscopic mechanisms in pore structures.

Microfluidic experiments at the pore scale, complemented by computational modelling, have been conducted to elucidate migration dynamics of two-phase fluids within porous structures (Cottin et al. 2010; Hu et al. 2018; Zhao et al. 2019; Zheng et al. 2017). Lenormand et al. (1988) investigated the interplay between capillary and viscous forces in oil-water displacement through numerical simulations and microfluidic experiments. Their work produced a seminal phase diagram correlating the capillary number (Ca) with the viscosity ratio (M). Based on the interaction of these forces, the invasion mechanisms were classified into three distinct types: (1) capillary fingering, (2) viscous fingering, or (3) stable displacement. Building on Lenormand et

© The Author(s) or their Institution(s)

al.'s phase diagram, Zhang et al. (2011) conducted water-wet micromodel displacement experiments to further investigate fluid flow behaviours. Their findings revealed that capillary fingering occurs at lower injection rates, irrespective of the viscosity ratio, while viscous fingering predominates when the invading fluid exhibits lower viscosity than the defending fluid. Experimental and simulation data indicate that the displacement efficiency of immiscible two-phase fluids spans a broad range, from 0.2 to 0.9, depending on the specific flow conditions and fluid properties (Zheng et al. 2017). Besides these primary factors, other important factors such as pore-scale heterogeneity, surface roughness, particle morphology, and wettability have been considered by researchers to further refine the classification of displacement patterns. The majority of these studies on immiscible displacement have been conducted under ambient conditions. However, many ongoing CO_2 sequestration projects, such as the Sleipner or Snøhvit project in Norway (Cavanagh and Haszeldine 2014; Hansen et al. 2013), In Salah project in Algeria (Rutqvist et al. 2010), and Shenhua project in China (Zhang et al. 2016), target depths exceeding 1000 meters, where pore pressures surpass 10 MPa. The physical property of CO_2 under these pressure conditions varies significantly (Zhong et al. 2024), leading to a shift to the dominant non-dimensional numbers. This raises an important unresolved question: to what extent the displacement mechanisms observed under low-pressure conditions are applicable to high-pressure scenarios encountered in deep geological sequestration.

The objective of the present study is to investigate displacement patterns and efficiency under varying CO_2 pressures. To address this issue, an advanced high-pressure microfluidic platform enabling real-time observation of CO_2 displacement patterns at the pore scale is developed. Microfluidic experiments of CO_2 flooding were conducted on a heterogeneous chip with broad coverage of pressure (i.e., from 1 bar to 16 MPa). Quantitative analyses were conducted to examine the changes in CO_2 saturation, displacement front length, and fractal dimension during the displacement process. This study not only provides a comprehensive and detailed description of the high-temperature and high-pressure microfluidic visualization system, but also reveals

© The Author(s) or their Institution(s)

novel insights into the fluid dynamics that are unobservable under traditional ambient conditions. The novel experimental framework established herein offers a significant advancement over conventional setups, enabling the observation of unique flow phenomena that are critical for optimizing industrial CO_2 geological storage operations across a wide range of pressure and temperature conditions.

2. Materials and Methods

2.1. High-pressure pore-visualisation system

Inspired by the previous works on multiphase flow at atmospheric pressure (Hu et al. 2019; Lu et al. 2025b; Zhan et al. 2021), the high-temperature and high-pressure visualization system is developed to investigate CO_2-water flow dynamics under extreme conditions, as illustrated in Figure 1. The system includes three high-pressure syringe pumps, two cylindrical storage vessels for CO_2 and deionised water, a micromodel, a high-pressure chamber, an imaging system, and various sensors. The micromodel, representing the porous medium, is housed in a high-pressure chamber equipped with high-temperature and high-pressure-resistant sapphire glass to enhance the operational pressure of the observation window. An injection pump introduces CO_2 into the water-saturated micromodel, while a back-pressure pump maintains a stable system pressure. A confining pump applies up to 50 MPa of pressure uniformly on both sides of the chip by injecting liquid into a sealed autoclave. The injection flow rate of this device ranges from 0.001 mL/min to 30 mL/min. Sensors monitor internal pressure and chamber temperature, ensuring precise control. The chamber and storage vessels are fitted with electric heating equipment capable of reaching temperatures up to 150 °C, enabling the system to replicate conditions found in deep geological environments for real-time visualisation of CO_2 displacement dynamics.

The imaging system features a video microscope (XCAMTOP4K) designed to capture detailed images of the micromodel's entire pore network. The microscope is

© The Author(s) or their Institution(s)

equipped with a SONY CMOS image sensor measuring 7.68 mm × 4.32 mm, providing a spatial resolution of 2 μm/pixel across the full field of view of the micromodels. The microscopy camera operates at a frame rate of 30 frames per second, with an image resolution of 3840 × 2160 pixels. Captured images are transmitted to connected computers for real-time recording and subsequent analysis, enabling precise visualisation and monitoring of pore-scale displacement dynamics.

2.2. Fabrication of heterogeneous microfluidic chips

Porous media micromodels were fabricated from high-strength glass using a lithography-etching technique (Cao et al. 2019). The fabricated microchannels demonstrate high-resolution patterning, with critical dimensions as small as 300 nm in depth and 2.5 μm in width. Our microfluidic chips measured 20 mm in length, 15 mm in width, and 20 μm in depth, with pore networks designed using irregular geometries of varying sizes to achieve a porosity of approximately 0.417 (Figure 1). Its pore structure is obtained from the image of a real core scanned by micro-CT, after undergoing image binarization and morphological processing. The fabrication process involved several key steps (Cao et al. 2019): (1) The glass substrate was cleaned and coated with a metal film. (2) A layer of photoresist was uniformly applied to the coated substrate, and a pre-designed image mask with micro-scale patterns was used. When exposed to UV light, the photoresist material in transparent areas would degrade, transferring the pattern onto the substrate. (3) The exposed areas were etched using a hydrofluoric acid solution to transfer the pattern from the photoresist to the glass, a process lasting approximately two hours. (4) Once the substrate was etched, the patterned glass was sealed by bonding two glass pieces under high temperature and pressure in a bonding machine. The resulting quasi-3D chip presented by Lu et al. (2025a) has a complex design in the horizontal direction, but its uniform and minimal depth cannot replicate intricate 3D flow structures. However, by neglecting cross-sectional details and focusing solely on flow parameters along the channel's length, the system can be reduced to a 1D flow system (Zhou et al. 2006). The chips featured

© The Author(s) or their Institution(s)

symmetrically arranged inlets and outlets in a binary tree structure to ensure uniform flow distribution across the pore network (Li et al. 2024; Zhan et al. 2021).

2.3. Experimental procedures

A clean micromodel was meticulously mounted in a high-pressure chamber. Deionised water was initially pumped continuously into the chamber using a confining pressure pump until the pressure reached 18 MPa, which was greater than the maximum displacement pressure. All experiments were conducted at room temperature (approximately 20 ± 0.5 °C), and heating equipment was not utilised. The micromodel was initially saturated with deionised water at a slow flow rate of 0.2 mL/min using the injection pressure pump at atmospheric pressure to ensure complete expulsion of air. Once the micromodel was fully saturated, the back-pressure pump was used to increase the system pressure to 16 MPa. Upon the inlet pressure reaching 16 MPa, valve B was closed while valve A was opened, after which CO_2 was injected into the microfluidic chip at a flow rate of 0.1 mL/min to displace the water. This flow rate was selected to ensure that the displacement process would be in the crossover zone between capillary and viscous figuring according to Lenormand's phase diagram (Lenormand et al. 1988). This allowed us to study the interaction of both forces. During this displacement process, the CMOS camera continuously captured images of CO_2 invasion morphologies until the CO_2 reached the micromodel's outlet. The back pressure was then progressively reduced to 12 MPa, 8 MPa, 5 MPa, 3 MPa, and finally 1 bar, with the microfluidic experiments at each pressure conducted following the same procedure. Each group of experiments was repeated 3 times, with a total of 18 experimental runs.

The fluid properties and experimental conditions at different pressures are listed in Table 1. The capillary number is defined as $Ca = \mu_{CO2} v/\sigma$, and the viscosity ratio is defined as $M = \mu_{CO2}/\mu_{water}$, where σ is the interfacial tension, v is the flow rate, μ_{CO2} and μ_{water} are the viscosities of CO_2 and water, respectively. As shown in Table 1, the density and viscosity of water change slightly when the pressure rises from 0.1

© The Author(s) or their Institution(s)

MPa to 16 MPa. However, the density of CO_2 increases by about 500 times, and its viscosity rises nearly six times. At 16 MPa, the density of CO_2 becomes much closer to that of water, while its viscosity is only one-tenth of water's viscosity. These significant variations in the physical properties of CO_2 under different pressure conditions have been largely neglected in previous microfluidic studies.

2.4. Image processing and analysis

To clearly delineate the interface between CO_2 and water, deionised water was dyed using an acid dye at a concentration of 0.2 wt % (weight percent). Due to the high solubility and low concentration of the dyes, and the minimal impact of its acidity on the surface tension and viscosity of deionized water (Beattie et al. 2014; Zhao et al. 2009), the effect of acidic dyes can be considered negligible. As shown in Figure 2a, in the original images, the dyed water appears dark, whereas CO_2 appears light, facilitating the distinction between the two phases through the application of an appropriate threshold. A MATLAB image processing algorithm was developed to convert the original images into binary format, as shown in Figure 2b. Using the binary images, the pixel area occupied by the invading CO_2, denoted as A_{CO2}, was quantified. This measurement was then used to calculate the CO_2 saturation S_g:

$$S_{\mathrm{g}} = \frac{A_{\mathrm{CO2}}}{A_{\mathrm{tol}}} \tag{1}$$

where A_{tol} is the total pixel area occupied by the pore space. The normalised length is determined as:

$$L_{\mathrm{inv}} = \frac{L_{\mathrm{max}}}{L_0} \tag{2}$$

where L_{max} is the furthest point of the displacement front of the fluid; and L_0 is the length of the chip. The fractal dimension D_{f} serves as a measure of pattern complexity, reflecting the ratio of detail change to scale change. The fractal dimension D_{f} was calculated using the standard box-counting method implemented in Fraclab, a MATLAB toolbox available at https://project.inria.fr/fraclab/. The method involved

© The Author(s) or their Institution(s)

using a variety of sized boxes to segment the image into distinct regions. As shown in Figure 2c, the image was divided into boxes, each measuring 1/8 of the size of the original image. The number of boxes occupied by the white regions, representing the CO_2 phase, was counted and denoted as N. D_f is calculated using the following (Wu et al. 2020):

$$D_f = \lim_{\varepsilon \to 0} \frac{\log N(\varepsilon)}{\log(\frac{1}{\varepsilon})} \quad (3)$$

where ε represents the length of a box.

3. Results and discussion

3.1. Comparison of displacement patterns

Figure 3 shows the invasion morphologies of CO_2 at breakthrough under various pressure conditions. At 1 bar, CO_2 primarily advances through the central main channel. At 3 MPa, flow paths expand, with the upper and lower channels becoming the primary conduits. At 5 MPa, in addition to the development of the main upper channel, several tributaries begin to form at the inlet. As pressure increases, these tributaries become more distinct and expansive, yet major flow channels remain present. As summarized in Table 1, the viscosity ratio of this experiment ranges from -1.02 to -1.83, and the capillary number ranges from -4.65 to -5.95, placing the experiment in the transition zone according to Lenormand's theory. At relatively low pressures, capillary forces predominantly govern the displacement of CO_2, propelling the fluid into larger throat pores and resulting in capillary fingering patterns. In contrast, at relatively high pressures, the viscous force of CO_2 exerts a more pronounced influence. This allows CO_2 to form multiple tributaries across the width of the micromodel at the inlet end. However, the presence of capillary forces ultimately causes CO_2 to break through the chip in the form of a dominant main flow channel. This phenomenon indicates that the crossover morphology from capillary to viscous fingering becomes the predominant displacement mechanism at elevated pressures. During the transition from low to high

© The Author(s) or their Institution(s)

pressure, the displacement patterns are influenced by an interplay of capillary and viscous forces.

3.2. Quantitative evaluation of displacement efficiency

Figure 4 illustrates the variation of S_g and D_f of invasion morphologies under different pressures at breakthrough. S_g exhibited a marked increase with rising pressure, particularly between 0.1 and 3 MPa, indicating a significant difference in CO_2 displacement efficiency compared to atmospheric pressure. This may be due to the significant differences in the physical properties of CO_2 under atmospheric pressure and high pressure. Concurrently, D_f also increased with pressure, reflecting the expansion of flow paths and increased complexity of flow patterns in the heterogeneous micromodel. This resulted in a concurrent increase in both D_f and S_g. Notably, when the pressure is between 3 MPa and 16 MPa, there is a minimal increase in S_g, whereas D_f shows a substantial rise. It indicates that while their displacement efficiency may not have differed significantly, there were substantial differences in the complexity of their invasion patterns.

Figure 5a illustrates the variation of S_g with T_{inv}, which was derived using min-max normalisation of the duration from the onset of invasion to breakthrough. In the early stage of invasion ($T_{inv} < 0.3$), S_g increased more rapidly at P=3 MPa and P=16 MPa compared to P=1 bar. This is attributed to the dominance of viscous forces at higher pressures, which promote the development of multiple finger branches, thereby enhancing CO_2 saturation. With the further increase in T_{inv}, the S_g of these cases increased steadily at relatively similar rates, but the S_g of P=16 MPa began to increase first. Toward the end of displacement ($T_{inv} > 0.9$), capillary forces became dominant at P=1 bar, leading to a smaller final saturation increase compared to higher pressures.

To further investigate the impact of the interaction between capillary and viscous forces on the invasion pattern, the variation of normalised invasion length L_{inv} with S_g is shown in Figure 5b. The results clearly demonstrate that L_{inv} decreased with increasing CO_2 pressure. This indicates that, for the same volume of injected CO_2, a

© The Author(s) or their Institution(s)

greater portion of the pore space was filled laterally under higher pressures, leading to a shorter invasion length in the longitudinal direction. This behaviour is a characteristic effect of viscous force, which also accounted for the higher S_g observed under elevated pressure conditions for the same injection time.

4. Conclusions

To advance the understanding of CO_2 behaviour in geological storage, a novel microfluidic experimental platform mimicking extreme underground conditions across a wide range of pressure and temperature conditions was developed to study CO_2-water displacement in heterogeneous porous structures. This platform achieves an experimental pressure of up to 50 MPa via a back-pressure system and enables observation of fluid changes through a high-pressure chamber equipped with an observation window. Microfluidic experiments conducted under varying pressures demonstrated that CO_2 displacement efficiency and patterns are significantly influenced by pressure variations. The physical properties of CO_2, such as density and viscosity, change substantially with pressure, impacting displacement mechanisms and efficiency. As pressure increased, the CO_2 saturation S_g and the fractal dimension D_f of the invasion morphology increased, indicating higher displacement efficiency and more complex flow patterns at elevated pressures. At low pressures and a flow rate of 0.1 mL/min, CO_2 displacement was primarily governed by capillary forces, resulting in capillary fingering patterns. In contrast, at higher pressures, the viscous force and capillary force jointly play a significant role, resulting in a crossover pattern. These findings highlight the importance of considering pressure effects on CO_2 displacement behaviour and efficiency in porous media, providing valuable insights for optimising geological sequestration processes. The present study fills this gap, providing new insights into the behaviour of CO_2 under high pressures and advancing the understanding of CO_2 displacement dynamics in geological storage scenarios. The subsequent stage of this research will systematically investigate the flow patterns across a wide range of flow rates to construct a complete phase diagram for high-pressure two-

© The Author(s) or their Institution(s)

phase flow. Furthermore, investigating the impact of cyclic loading-induced rock fatigue damage (Hong et al. 2024; Liu and Dai 2018) on the flow structure of two-phase fluids will be a key focus of our future research, which is critical for understanding the long-term stability of CO_2 geological storage.

Acknowledgements

The authors gratefully acknowledge the financial supports provided by National Natural Science Foundation of China (52122906, 52238001 and 52306205), Donghai Laboratory (DH-2022ZY0008).

Data availability

All data, models, or codes that support the findings of this study are available from the corresponding author upon reasonable request.

Draft

Competing interests

The authors declare that they have no known competing financial interests or personal relationships that could have appeared to influence the work reported in this paper.

References

Bachu, S., and D. Bennion. 2009. Interfacial tension between CO_2, freshwater, and brine in the range of pressure from (2 to 27) MPa, temperature from (20 to 125) °C, and water salinity from (0 to 334 000) mg • l^{-1}. Journal of Chemical and Engineering Data, **54**, doi: 10.1021/je800529x.

Beattie, J.K., Djerdjev, A.M., Gray-Weale, A., Kallay, N., Lützenkirchen, J., Preočanin, T. and Selmani, A. 2014. pH and the surface tension of water. Journal of Colloid and Interface Science, **422**: 54-57.

Berg, S. and Ott, H. 2012. Stability of CO_2–brine immiscible displacement. International Journal of Greenhouse Gas Control, **11**: 188-203.

Cao, S.C., Jung, J. and Radonjic, M. 2019. Application of microfluidic pore models for flow, transport, and reaction in geological porous media: from a single test bed to multifunction real-time

© The Author(s) or their Institution(s)

analysis tool. Microsystem Technologies, **25**(11): 4035-4052.

Cavanagh, A.J. and Haszeldine, R.S. 2014. The Sleipner storage site: Capillary flow modeling of a layered CO_2 plume requires fractured shale barriers within the Utsira Formation. International Journal of Greenhouse Gas Control, **21**: 101-112.

Cottin, C., Bodiguel, H. and Colin, A. 2010. Drainage in two-dimensional porous media: From capillary fingering to viscous flow. Physical Review E, **82**(4): 046315.

Doughty, C. 2010. Investigation of CO_2 Plume Behavior for a Large-Scale Pilot Test of Geologic Carbon Storage in a Saline Formation. Transport in Porous Media, **82**(1): 49-76.

Goodman, A., Hakala, A., Bromhal, G., Deel, D., Rodosta, T., Frailey, S., Small, M., Allen, D., Romanov, V., Fazio, J., Huerta, N., McIntyre, D., Kutchko, B. and Guthrie, G. 2011. U.S. DOE methodology for the development of geologic storage potential for carbon dioxide at the national and regional scale. International Journal of Greenhouse Gas Control, **5**(4): 952-965.

Hansen, O., Gilding, D., Nazarian, B., Osdal, B., Ringrose, P., Kristoffersen, J.-B., Eiken, O. and Hansen, H. 2013. Snøhvit: The history of injecting and storing 1 Mt CO_2 in the fluvial Tubåen Fm. Energy Procedia, **37**: 3565-3573.

Ho, C.M.B., Sun, Q., Teo, A.J.T., Wibowo, D., Gao, Y., Zhou, J., Huang, Y., Tan, S.H. and Zhao, C.-X. 2020. Development of a Microfluidic Droplet-Based Microbioreactor for Microbial Cultivation. ACS Biomaterials Science & Engineering, **6**(6): 3630-3637.

Hong, Y., Wang, X., Wang, L., Kang, G. and Gao, Z. 2024. High-cycle shakedown, ratcheting and liquefaction behavior of anisotropic granular material with fabric evolution: Experiments and constitutive modelling. Journal of the Mechanics and Physics of Solids, **187**.

Hu, R., Wan, J., Kim, Y. and Tokunaga, T.K. 2017. Wettability impact on supercritical CO_2 capillary trapping: Pore-scale visualization and quantification. Water Resources Research, **53**(8): 6377-6394.

Hu, R., Wan, J., Yang, Z., Chen, Y.-F. and Tokunaga, T. 2018. Wettability and Flow Rate Impacts on Immiscible Displacement: A Theoretical Model. Geophysical Research Letters, **45**(7): 3077-3086.

Hu, R., Zhou, C.-X., Wu, D.-S., Yang, Z. and Chen, Y.-F. 2019. Roughness Control on Multiphase Flow in Rock Fractures. Geophysical Research Letters, **46**(21): 12002-12011.

Huang, P., Shen, L., Gan, Y., Maggi, F., El-Zein, A. and Pan, Z. 2019. Atomistic Study of Dynamic Contact Angles in CO_2 − Water − Silica System. Langmuir, **35**(15): 5324-5332.

Jiang, R., Dai, F., Liu, Y. and Li, A. 2021. Fast Marching Method for Microseismic Source Location in Cavern-Containing Rockmass: Performance Analysis and Engineering Application. Engineering, **7**(7): 1023-1034.

Juanes, R., MacMinn, C.W. and Szulczewski, M.L. 2010. The Footprint of the CO_2 Plume during Carbon Dioxide Storage in Saline Aquifers: Storage Efficiency for Capillary Trapping at the Basin Scale. Transport in Porous Media, **82**(1): 19-30.

Kim, Y., Wan, J., Kneafsey, T. and Tokunaga, T. 2012. Dewetting of Silica Surfaces upon Reactions with Supercritical CO_2 and Brine: Pore-Scale Studies in Micromodels. Environmental Science & Technology, **46**: 4228-35.

Lenormand, R., Touboul, E. and Zarcone, C. 1988. Numerical models and experiments on immiscible displacements in porous media. Journal of Fluid Mechanics, **189**: 165-187.

Li, A., Liu, Y., Dai, F., Liu, K. and Wei, M. 2020. Continuum analysis of the structurally controlled displacements for large-scale underground caverns in bedded rock masses. Tunnelling and

© The Author(s) or their Institution(s)

Underground Space Technology, **97**: 103288.

Li, G., Zhan, L., Zhang, Z., Zhang, S. and Feng, S. 2024. Pore network modeling of capillary barrier effects: impact of pore sizes. **61**(1): 174-182.

Liu, Y. and Dai, F. 2018. A damage constitutive model for intermittent jointed rocks under cyclic uniaxial compression. International Journal of Rock Mechanics and Mining Sciences, **103**: 289-301.

Liu, Y., Sun, L., Zhang, H., Shang, L. and Zhao, Y. 2021. Microfluidics for Drug Development: From Synthesis to Evaluation. Chemical Reviews, **121**(13): 7468-7529.

Lu, Z., Wang, L., Guo, Z., Hong, Y. and Zhang, L. 2025a. The microfluidic in geo-energy resources: Current advances and future perspectives. Advances in Geo-Energy Research, **16**(2): 171-180.

Lu, Z., Zeng, C., Zhang, Y. and Lu, H. 2025b. Study of the pore size influence on infiltration of porous media considering capillary effect. Capillarity, **14**(1): 1-12.

NIST Chemistry WebBook: http://webbook.nist.gov/chemistry/, October 28, 2016.

Rutqvist, J., Vasco, D.W. and Myer, L. 2010. Coupled reservoir-geomechanical analysis of CO_2 injection and ground deformations at In Salah, Algeria. International Journal of Greenhouse Gas Control, **4**(2): 225-230.

Saadat, M., Yang, J., Dudek, M., Øye, G. and Tsai, P.A. 2021. Microfluidic investigation of enhanced oil recovery: The effect of aqueous floods and network wettability. Journal of Petroleum Science and Engineering, **203**: 108647.

Song, Y., Jiang, L., Liu, Y., Yang, M., Zhao, Y., Zhu, N., Dou, B. and Abudula, A. 2012. An experimental study on CO_2/water displacement in porous media using high-resolution Magnetic Resonance Imaging. International Journal of Greenhouse Gas Control, **10**: 501-509.

Song, Y., Zhao, C., Chen, M., Chi, Y., Zhang, Y. and Zhao, J. 2020. Pore-scale visualization study on CO_2 displacement of brine in micromodels with circular and square cross sections. International Journal of Greenhouse Gas Control, **95**: 102958.

Umar, B.A., Gholami, R., Raza, A., Downey, W.S., Sarmadivaleh, M., Shah, A.A. and Nayak, P. 2020. A Study on the Surface Wettability of Clastic Rocks with Potential Application for CO2 Storage Sites. Natural Resources Research, **29**(3): 2051-2061.

Wang, T., Zhang, L., Sun, L., Zhou, R., Dong, B., Yang, L., Li, Y., Zhao, J. and Song, Y. 2021. Methane recovery and carbon dioxide storage from gas hydrates in fine marine sediments by using CH_4/CO_2 replacement. Chemical Engineering Journal, **425**: 131562.

Wang, Y., Zhang, C., Wei, N., Oostrom, M., Wietsma, T.W., Li, X. and Bonneville, A. 2013. Experimental Study of Crossover from Capillary to Viscous Fingering for Supercritical CO_2–Water Displacement in a Homogeneous Pore Network. Environmental Science & Technology, **47**(1): 212-218.

Wu, J., Jin, X., Mi, S. and Tang, J. 2020. An effective method to compute the box-counting dimension based on the mathematical definition and intervals. Results in Engineering, **6**: 100106.

Yao, Y., Chen, D. and Yin, Z. 2022. On the Importance of DIOX Concentration in Promoting CH_4 Hydrate Formation: A Thermodynamic and Kinetic Investigation. Fuel, **324**: 124355.

Yu, H., Wang, S., Yang, H., Yang, Y., Zhang, J., Wang, Y., Yang, W. and Lu, J. 2023. A Systematic Method to Investigate the EOR Mechanism of Nanospheres: Laboratory Experiments from Core to Micro Perspective. Energy & Fuels, **37**.

Zeng, C., Zhang, Y., Lu, H. and Lu, Z. 2025. Simulation of CO_2-water two-phase fluid displacement characteristics based on the phase field method. Deep Underground Science and Engineering: 1-14.

© The Author(s) or their Institution(s)

Zhan, L., Li, G., Bate, B. and Chen, Y. 2021. A preliminary exploration of the micro-scale behaviour of capillary barrier effect using microfluidics. Géotechnique, **73**(6): 553-560.

Zhang, C., Oostrom, M., Wietsma, T.W., Grate, J.W. and Warner, M.G. 2011. Influence of Viscous and Capillary Forces on Immiscible Fluid Displacement: Pore-Scale Experimental Study in a Water-Wet Micromodel Demonstrating Viscous and Capillary Fingering. Energy & Fuels, **25**(8): 3493-3505.

Zhang, K., Xie, J., Li, C., Hu, L., Wu, X. and Wang, Y. 2016. A full chain CCS demonstration project in northeast Ordos Basin, China: operational experience and challenges. International Journal of Greenhouse Gas Control, **50**: 218-230.

Zhang, N., Li, S., Chen, L., Guo, Y. and Liu, L. 2024. Study of gas-liquid two-phase flow characteristics in hydrate-bearing sediments. Energy, **290**: 130215.

Zhang, X., Li, L., Su, Y., Da, Q.a., Fu, J., Wang, R. and Chen, F. 2023. Microfluidic investigation on asphaltene interfaces attempts to carbon sequestration and leakage: Oil-CO_2 phase interaction characteristics at ultrahigh temperature and pressure. Applied Energy, **348**: 121518.

Zhao, B., MacMinn, C.W., Primkulov, B.K., Chen, Y., Valocchi, A.J., Zhao, J., Kang, Q., Bruning, K., McClure, J.E., Miller, C.T., Fakhari, A., Bolster, D., Hiller, T., Brinkmann, M., Cueto-Felgueroso, L., Cogswell, D.A., Verma, R., Prodanović, M., Maes, J., Geiger, S., Vassvik, M., Hansen, A., Segre, E., Holtzman, R., Yang, Z., Yuan, C., Chareyre, B. and Juanes, R. 2019. Comprehensive comparison of pore-scale models for multiphase flow in porous media. Proceedings of the National Academy of Sciences, **116**(28): 13799-13806.

Zhao, J., Luo, Z., Ni, M. and Cen, K. 2009. Dependence of Nanofluid Viscosity on Particle Size and pH Value. Chinese Physics Letters, **26**(6): 066202.

Zheng, X., Mahabadi, N., Yun, T.S. and Jang, J. 2017. Effect of capillary and viscous force on CO_2 saturation and invasion pattern in the microfluidic chip. Journal of Geophysical Research: Solid Earth, **122**(3): 1634-1647.

Zhong, H., Wang, Z., Zhang, Y., Suo, S., Hong, Y., Wang, L. and Gan, Y. 2024. Gas storage in geological formations: A comparative review on carbon dioxide and hydrogen storage. Materials Today Sustainability, **26**: 100720.

Zhou, L., Wang, K., Tan, W., Chen, Y., Zuo, X., Wen, J., Liu, B., Tang, H., He, L. and Yang, X. 2006. Quantitative Intracellular Molecular Profiling Using a One-Dimensional Flow System. Analytical Chemistry, **78**(17): 6246-6251.

Caption of Tables

Table 1. Summary of fluid properties and experimental conditions.

Table 1. Summary of fluid properties and experimental conditions.

Property	Values					
Pressure (MPa)	0.10	3.00	5.00	8.00	12.00	16.00

© The Author(s) or their Institution(s)

Density of CO_2 (kg/m3)[a]	1.82	66.16	140.65	827.71	878.10	911.37
Density of water (kg/m3)[a]	998.21	999.53	1000.44	1001.80	1003.59	1005.37
Viscosity of CO_2 (mPa·s)[a]	0.015	0.015	0.017	0.076	0.086	0.094
Viscosity of water (mPa·s)[a]	1.002	1.001	1.000	0.999	0.998	0.997
Interfacial tension (mN/m)[b, c]	72.80	52.95	39.20	29.10	25.10	23.69
Contact angle (°) [d]	10	14	17	21	25	27
Flow rate, Q (mL/min)	0.1					
Temperature (°C)	20±0.5					
Viscosity ratio, $\log_{10}M$	-1.83	-1.82	-1.78	-1.12	-1.06	-1.02
Capillary number, $\log_{10}Ca$	-5.95	-5.80	-5.62	-4.84	-4.71	-4.66

[a]The density and viscosity of CO_2 and water were obtained from phase diagram at the NIST (National Institute of Standards and Technology, USA) Chemistry WebBook (2016).

[b, c]The interfacial tension for CO_2 and water was obtained from Bachu and Bennion (2009) and Huang et al. (2019).

[d]The contact angles of CO_2/water/quartz systems were obtained from Umar et al. (2019).

Draft

Caption of Figures

Fig. 1. High-temperature and high-pressure transparent pore-visualization system.

Fig. 2. Microfluidic image processing workflow. (a) Original image; (b) processed binary image with L_{max} definition; (c) fractal dimension calculation using the box-counting method in Fraclab (a MATLAB Toolbox, https://project.inria.fr/fraclab/).

Fig. 3. Displacement patterns for different pressure at the breakthrough. (a) P=1 bar; (b) P=3 MPa; (c) P=5 MPa; (d) P=8 MPa; (e) P=12 MPa; (f) P=16 MPa. The flow direction within chips is from right to left.

Fig. 4. Variation of CO_2 saturation (S_g) and fractal dimension (D_f) of invasion morphologies with pressure at breakthrough. Error bars indicate relative error.

Fig. 5. (a) Variation of CO_2 saturation S_g with the normalised time T_{inv}. T_{inv} is derived

© The Author(s) or their Institution(s)

through min-max normalization of the time elapsed from invasion onset to breakthrough. (b) Variation of the normalised length L_{inv} with CO_2 saturation S_g.

Draft

© The Author(s) or their Institution(s)

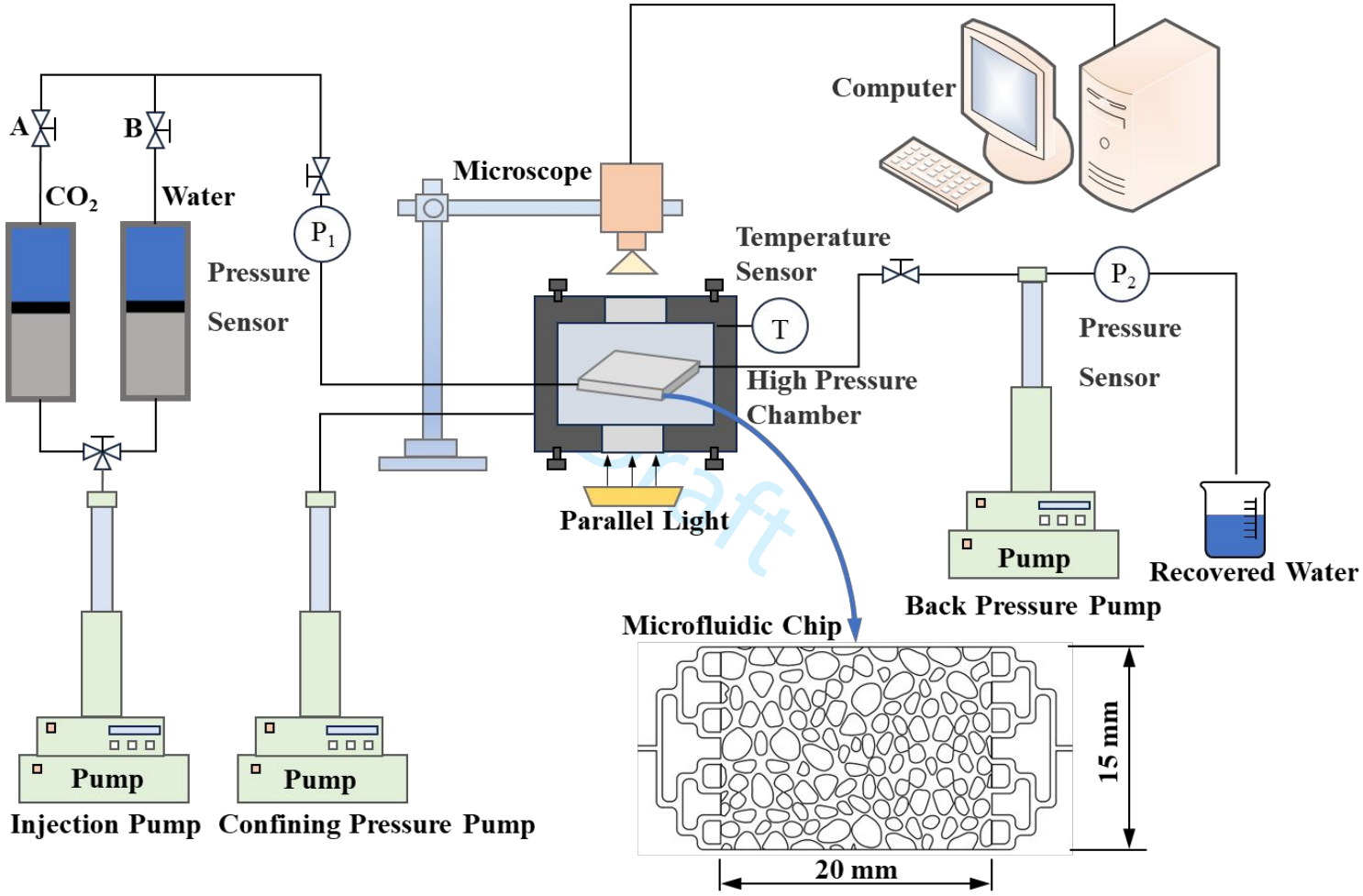

Fig. 1. High-temperature and high-pressure transparent pore-visualization system.

© The Author(s) or their Institution(s)

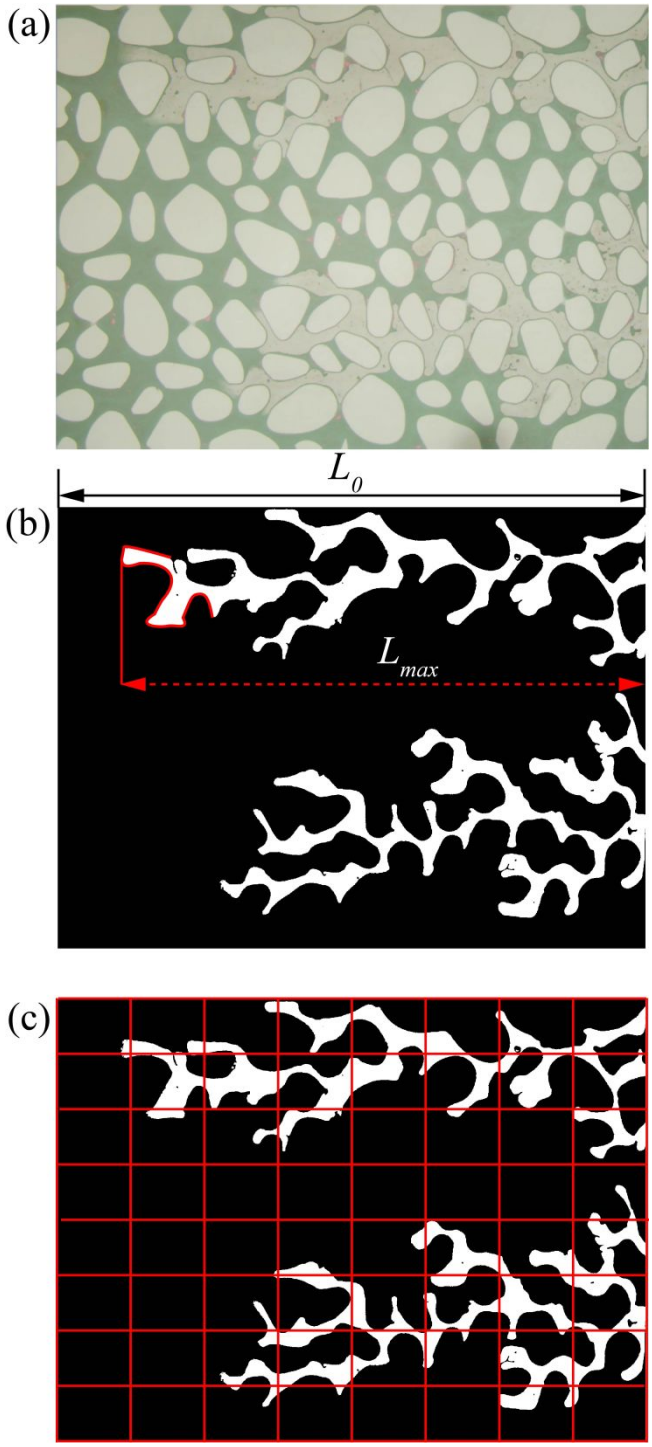

Fig. 2. Microfluidic image processing workflow. (a) Original image; (b) processed binary image with L_{max} definition; (c) fractal dimension calculation using the box-counting method in Fraclab (a MATLAB Toolbox, https://project.inria.fr/fraclab/).

© The Author(s) or their Institution(s)

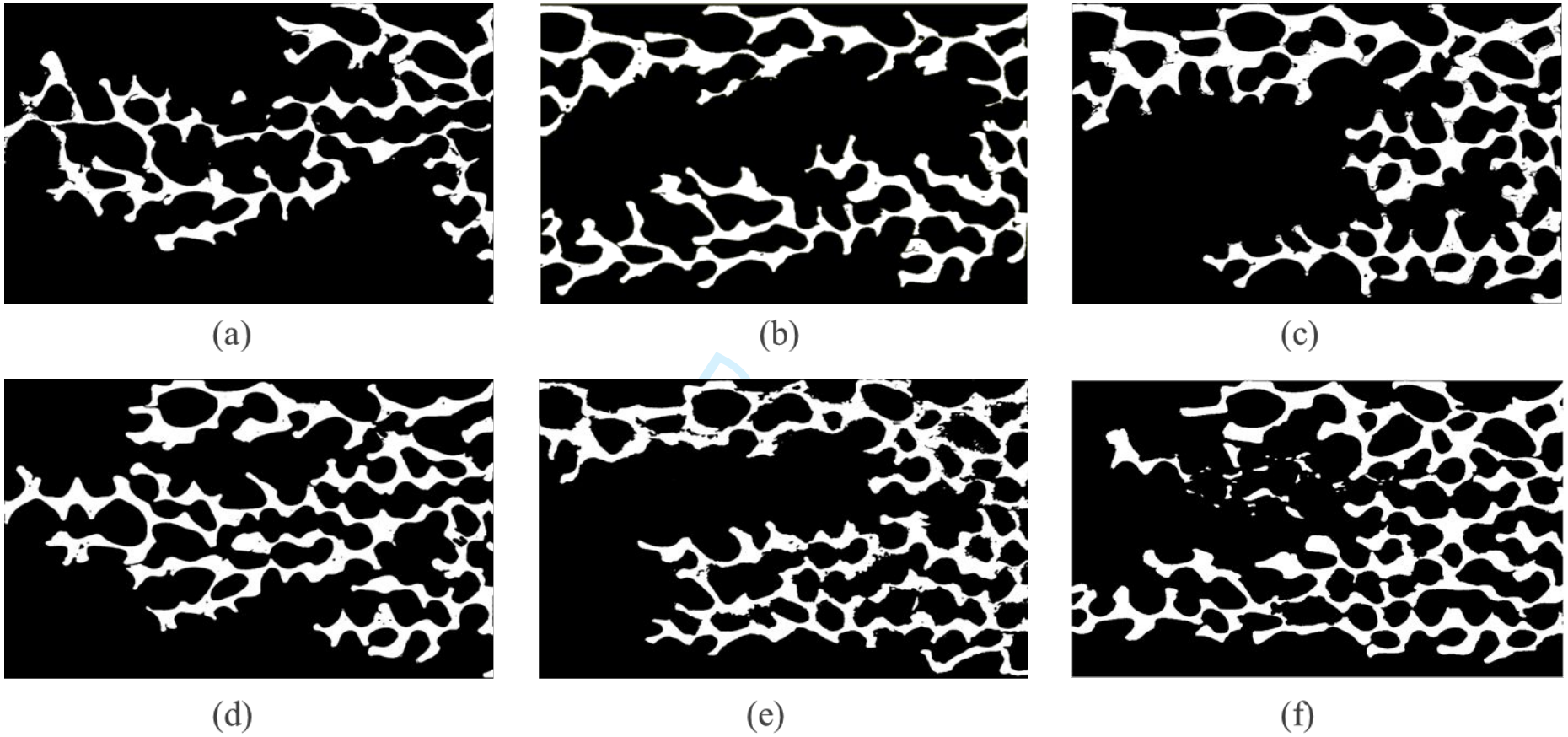

Fig. 3. Displacement patterns for different pressure at the breakthrough. (a) P=1 bar; (b) P=3 MPa; (c) P=5 MPa; (d) P=8 MPa; (e) P=12 MPa; (f) P=16 MPa. The flow direction within chips is from right to left.

© The Author(s) or their Institution(s)

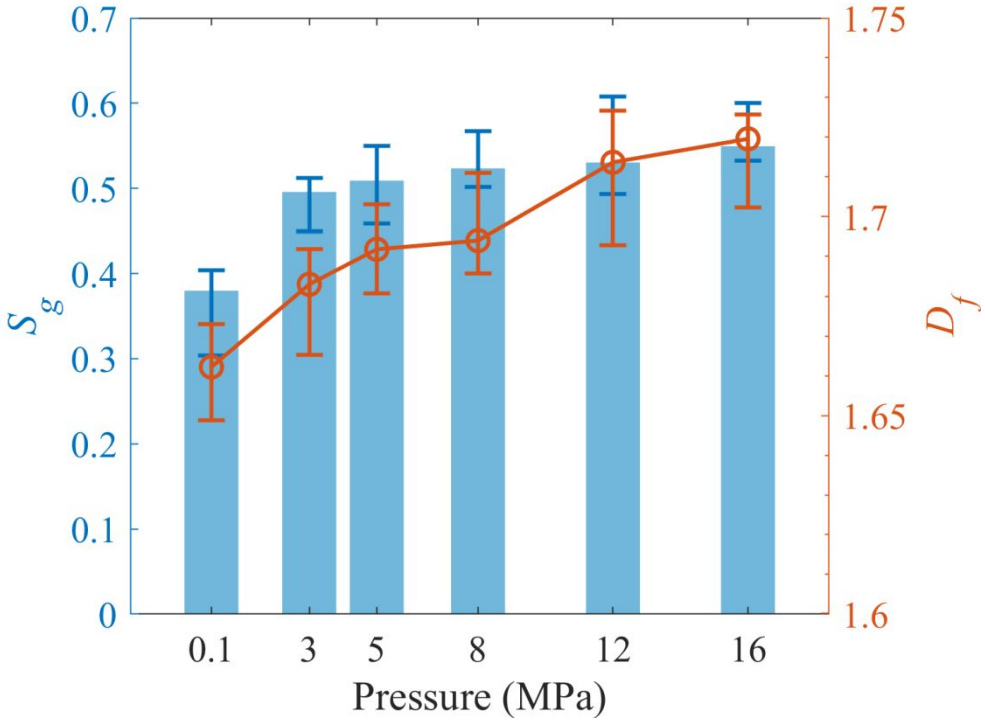

Fig. 4. Variation of CO_2 saturation (S_g) and fractal dimension (D_f) of invasion morphologies with pressure at breakthrough. Error bars indicate relative error.

© The Author(s) or their Institution(s)

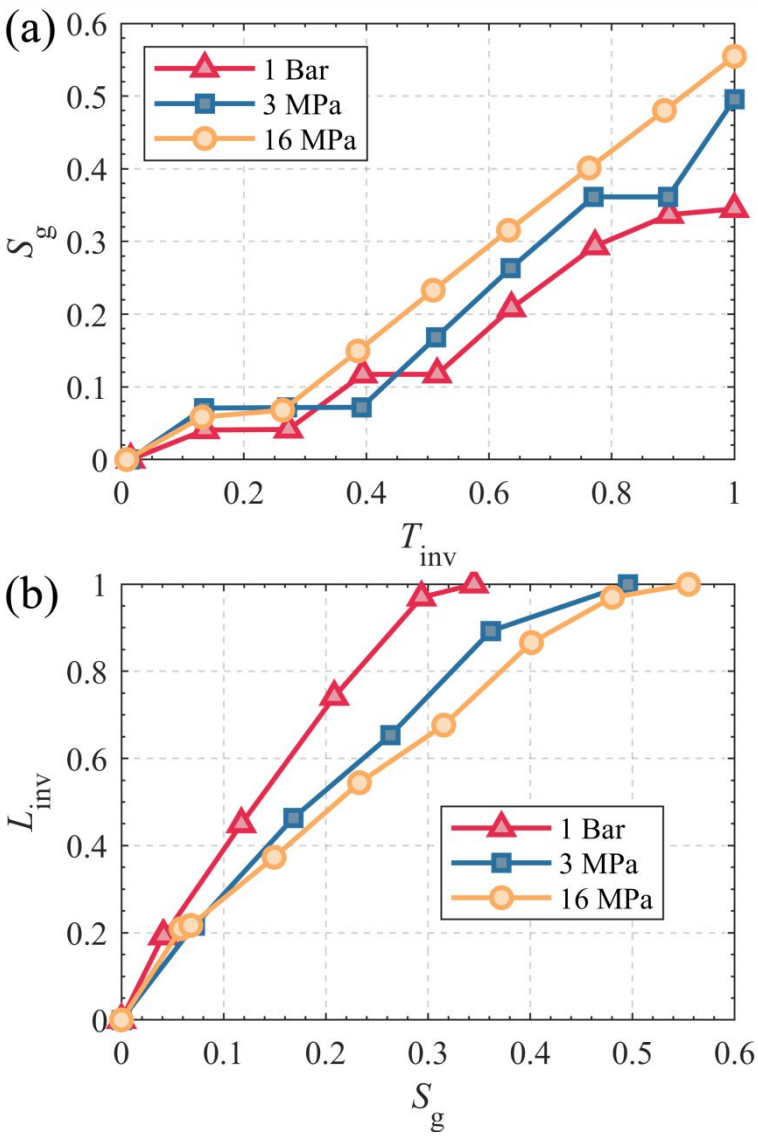

Fig. 5. (a) Variation of CO_2 saturation S_g with the normalised time T_{inv}. T_{inv} is derived through min-max normalization of the time elapsed from invasion onset to breakthrough. (b) Variation of the normalised length L_{inv} with CO_2 saturation S_g.

© The Author(s) or their Institution(s)